

# Photocatalytic properties of titania/porous carbon fibers composites prepared by self-template method

Feng Teng · Guozhi Zhang · Youqing Wang ·  
Caitian Gao · Zhenxing Zhang · Erqing Xie

Received: 14 September 2014 / Accepted: 13 January 2015 / Published online: 23 January 2015  
© Springer Science+Business Media New York 2015

**Abstract** Photocatalytic degradation is one of the most popular routes applied in the wastewater treatments. But the most used nanoparticle photocatalysts have a serious drawback that the particles are not easy to precipitate and recover from water, which seriously hinder its applications. In this study, titania/porous carbon fibers composite prepared by a simple self-template method with micro-meter long carbon fibers and titania nanoparticles as precursors was investigated to solve these issues. The obtained composite can precipitate from the solution easily, which is the major reason that it can be used in actual applications. We found that the titania particles, as catalysts, could enhance the reaction between carbon fibers and oxygen during the calcinations process, and as a template, would determine the size and position of the pores on the fibers surface simultaneously. Due to the unique porous structure, the titania/porous carbon fibers composite shows considerable adsorption and high photocatalytic activity. Combining the advantages of titania and carbon fibers, the composite can be also applied in many other fields, such as water splitting for hydrogen and lithium ion batteries.

## Introduction

With industrialization and population growth, the environmental contamination, especially caused by organic pollutants, becomes an increasingly severe problem around the world. And the possession of clean water determines whether an area is suitable for human habitation. In the past decades, various techniques, such as chemical precipitation, adsorption, biological removal, reverse osmosis, photocatalysis and membrane, have been studied for the removal of organic pollutants from wastewater [1–3]. Among these approaches, adsorption and photocatalytic degradation are the two most popular routes.

As the easiest method of decontamination, adsorption has been considered as one of the most promising technologies for organic removal in terms of cost, simplicity of design, and operation. A wide range of adsorbent materials such as activated carbon, clay, silica gel, and cellulose have been reported. Activated carbon stands out among these adsorbents owing to its extensive pore surface area, interconnected pore structure, unique surface chemistry [4–6]. Unfortunately, merely physical adsorption is insufficient for pollutants removal because the toxic pollutants cannot be effectively converted to other non-toxic substances. The adsorbents need to be replaced when they reach the saturation adsorption, which leads to a new problem that how to deal with these adsorbents. However, due to its unique performance, the adsorption process could be considered as a necessary factor to increase the encounter probability between the pollutants and catalysts when the pollutants are degraded by catalysis [7, 8].

As a green technology, heterogeneous photocatalysis by semiconductor materials has gained increasing interest because it is widely applied in environmental purification

---

Feng Teng and Guozhi Zhang have contributed equally to this work

**Electronic supplementary material** The online version of this article (doi:10.1007/s10853-015-8857-8) contains supplementary material, which is available to authorized users.

---

F. Teng · G. Zhang · Y. Wang · C. Gao · Z. Zhang (✉) ·  
E. Xie (✉)

School of Physical Science and Technology, Lanzhou  
University, Lanzhou 730000, People's Republic of China  
e-mail: zhangzx@lzu.edu.cn

E. Xie  
e-mail: xieeq@lzu.edu.cn

(non-selective process) and selective organic transformations to fine chemicals in both gas and liquid phases [9–11]. Among the various semiconductor materials, titanium dioxide ( $\text{TiO}_2$ ) has been extensively studied and commonly applied as a photocatalyst in environmental cleaning because of its superior photocatalytic activity, high photo-stability, chemical resistance, low cost, abundance, and environmentally benign nature [12, 13]. However, the photocatalytic activity of  $\text{TiO}_2$  is greatly restricted by its low quantum efficiency in photocatalytic reactions and ineffective utilization of visible light, which result from its high recombination of photo-generated electron–hole pairs and wide band gap (3.2 eV for anatase), respectively [14–18]. Moreover, although nanosized  $\text{TiO}_2$  catalyst has high photocatalytic activity among the current popular catalysts, it still presents a drawback that the powders are not easy to precipitate and recover from water, which are detrimental to their regeneration and reuse [19]. In order to realize photocatalytic degradation of pollutants used in large-scale water treatment facilities, the immobilized problem of  $\text{TiO}_2$  must be solved. In recent years, many researchers have been devoted to immobilize  $\text{TiO}_2$  nanostructures on different substrate materials to hinder agglomeration [20]. For example, Wang et al. have demonstrated carbon fibers (CFs) can be used as substrate for growing  $\text{TiO}_2$  nanosheets because CFs are flexible, conductive, and stable in corrosive conditions [21]. In addition, synergistic effect between  $\text{TiO}_2$  and carbon could greatly retard the recombination of photo-induced electrons and holes, leading to the enhanced photocatalytic performance of  $\text{TiO}_2$  [22]. To utilize this synergistic effect, many related hybrid structures have been investigated, such as graphene/ $\text{TiO}_2$  composites, [23] carbon nanotube (CNT)– $\text{TiO}_2$  composites, [24]  $\text{TiO}_2$ /AC composites ( $\text{TiO}_2$ -loaded on activated carbon) [25, 26], and so on [27–29]. In view of the high cost of graphene and CNT, carbon fiber as an industrial product is an excellent candidate material to support the catalysts. But CF has lower surface area than graphene, CNT and AC due to no significant nanostructures on its surface, which restricts its potential as catalyst supporter.

In this paper, we report a facile preparation method of  $\text{TiO}_2$ /porous CFs composite based on self-template method. The highlights of this work are that the CFs would be etched into the porous structure by the oxygen in air at high temperature when the  $\text{TiO}_2$  particles were loaded on its surface. This  $\text{TiO}_2$ /porous CFs composite shows unique characteristics such as excellent adsorption and high photocatalytic activities. These findings afford the convenient optimization for the design of  $\text{TiO}_2$ -based photocatalytic device, which would achieve the application of the photocatalytic degradation of the organic pollutants in wastewater.

## Experimental section

### Synthesis of samples

All reagents were of analytical grade and used without further purification. The carbon fibers calcined at 1600 °C in argon atmosphere (Blue Star (Group) Co., Ltd., Lanzhou) were used in our experiment and the length of the CFs was unified to about 1 mm. The preparation process of the composite is described as below. P25 powders (1 g, Degussa) and additives (polyethylene glycol or acetic acid) were dissolved into 20 mL deionized water with stirring for 1 h to get a homogeneous P25 solution. Subsequently, 0.5 g prepared CFs were added into the above solution and magnetically stirred for another 1 h. Then the solution was dried and the P25/CFs composite was obtained. Then the P25/CFs composites were annealed with a ramp rate of 2 °C  $\text{min}^{-1}$  for 2 h at 400, 450, 500, 550, and 600 °C, respectively.

### Characterization of samples

Morphologies were examined by field emission scanning electron microscopy (FESEM, Hitachi S-4800). Raman spectra were recorded on JY-HR800 Raman spectroscopy with a 532-nm laser line from the yttrium aluminum garnet laser. The crystal phases were determined by X-ray diffraction analyzer (XRD, PANalytical X'Pert) with Cu-K $\alpha$  radiation ( $\lambda = 1.5418 \text{ \AA}$ ). X-ray photoelectron spectra (XPS) were recorded with a Kratos AXIS Ultra DLD XPS instrument equipped with an Al K $\alpha$  source at  $10^{-9}$  Torr. The surface area and porosity of the products were measured by the nitrogen adsorption–desorption isotherm and Barrett–Joyner–Halenda (BJH) methods on a Micromeritics ASAP 2020M accelerated surface area and porosimetry system.

### Catalytic activity measurements

The photocatalytic activity was evaluated by the time evolution of photodegradation of rhodamine B (RhB). During the measurement of the photocatalytic performance, the amount of photocatalyst was kept at the same in all tests. 50-mg photocatalyst and 50 mL of RhB solution ( $10 \text{ mg L}^{-1}$ ) were placed into a crystallizing dish (100 mL). The suspension was magnetically stirred in dark conditions for 60 min to ensure the adsorption/desorption equilibrium. After the dark treatment, the solution was subsequently irradiated by a 175 W tungsten halogen lamp with magnetic stirring at ambient temperature. During the irradiation, 4 mL of the solution was taken from the reactor at a scheduled interval and filtered with pore size = 1  $\mu\text{m}$  cellulose acetate membrane filters to remove the residual

catalyst. The filtrate was analyzed by recording variations at the wavelength of maximal absorption ( $\lambda = 554$  nm) in the UV–visible spectrum of RhB using a TU-1901 spectrophotometer.

## Results and discussion

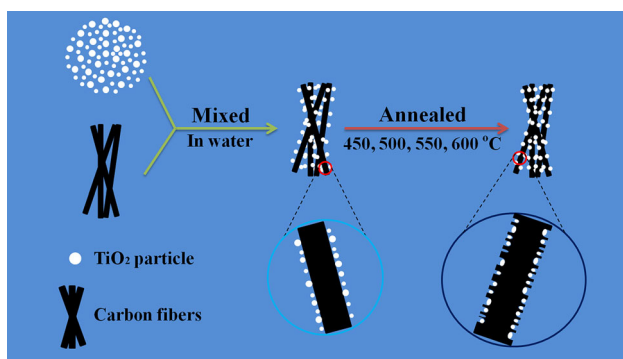
### Morphology, components, and phase analysis

Scheme 1 shows a schematic representation of the formation process of the TiO<sub>2</sub>/porous CFs composite by the self-template method. The SEM images of the original P25 nanoparticles and CFs are shown in Fig. S1 (Supporting information). It can be seen that the P25 nanoparticles with average diameter of 25 nm are agglomerate in a certain degree, and the CFs have uniform size of 8  $\mu\text{m}$  in diameter and smooth surface. Figure 1 shows the SEM images of the CFs with the P25 particles loaded on its surface. In order to make the P25 particles on the CFs surface more dispersed and reduce the agglomerations, a common dispersant (polyethylene glycol, PEG) was added into the P25 aqueous solution. Figure 1a shows the morphology of the P25/CFs composite with PEG as additive. Huge P25 clusters are formed on the CFs surface because P25 can easily adsorb on PEG molecules and then adhere to CFs, which leads to more serious agglomeration than that without additive (as shown in Fig. 1b). Considering the above problem, acetic acid (CH<sub>3</sub>COOH) was added into the P25 solution to replace PEG, because of the change of zeta potential on the TiO<sub>2</sub> surface in acid solution and the existence of titanium acetate, which can enhance the dispersion of P25 particles in aqueous solution [30, 31]. Figure 1c and d displays the SEM images of P25/CFs composites with CH<sub>3</sub>COOH as additive. Although few P25 clusters are still present, the distribution of P25 particles is obviously more uniform than those without additive and with PEG as additive. Figure 2 demonstrates the high-resolution SEM images of

the P25/CFs composites with PEG and CH<sub>3</sub>COOH as additives, respectively. Due to the PEG coating, the P25 nanoparticles are not very clear, as shown in Fig. 2a and b, which confirms the inference mentioned above. Compared with the sample using PEG as additive, the P25 particles of the sample using CH<sub>3</sub>COOH as additive are distributed more uniformly, as shown in Fig. 2c and d. Therefore, a TiO<sub>2</sub>/CFs composite is obtained with the relatively uniform distribution of P25 particles.

To further enhance the interaction between P25 and CFs, the as-prepared P25/CFs composites were calcined for 2 h at 400, 450, 500, 550, and 600  $^{\circ}\text{C}$ , respectively. The corresponding samples are labeled as S400, S450, S500, S550, and S600, respectively. For the S400 sample (Fig. 3a), the surface of CFs still remains the original morphology while it becomes smooth after calcination at 450  $^{\circ}\text{C}$  (Fig. 3c). A unique porous structure appears when the calcination temperature reaches 500  $^{\circ}\text{C}$  (Fig. 3e) or higher (550  $^{\circ}\text{C}$  of Fig. 3g, 600  $^{\circ}\text{C}$  of Fig. 3i). The contour of their pores coincides with the contour of P25 clusters, as shown in Fig. S2 (Supporting information). In order to verify the role of TiO<sub>2</sub> particles, the CFs without P25 particles attached were also calcined at above mentioned temperatures. From their SEM images (400  $^{\circ}\text{C}$  of Fig. 3b, 450  $^{\circ}\text{C}$  of Fig. 3d, 500  $^{\circ}\text{C}$  of Fig. 3f, 550  $^{\circ}\text{C}$  of Fig. 3h, 600  $^{\circ}\text{C}$  of Fig. 3j), it can be observed that the diameter of the CFs is decreased and few pores appear on the surface as the temperature increases, and only some flat pits are formed when the calcination temperature is 600  $^{\circ}\text{C}$ . Therefore, we can conclude that the TiO<sub>2</sub> particles can act as catalyst to enhance the etch reaction between CFs and oxygen. At the same time, it can act as template to determine the shape of the pores. So far, a TiO<sub>2</sub>/porous CFs composite is obtained, and the formation mechanism will be discussed later.

The characteristics of the TiO<sub>2</sub>/porous CFs were further investigated with the N<sub>2</sub> adsorption/desorption analysis. The typical result is shown in Fig. S3 (Supporting information), and the relative BET data are shown in Table 1. From Table 1, it can be seen that the special surface area of the original TiO<sub>2</sub>/CFs composite is about 41.38 m<sup>2</sup> g<sup>-1</sup>. After annealing at 400 and 450  $^{\circ}\text{C}$ , the surface area of the composite dropped obviously because the surface of CFs is etched by the oxygen in air and becomes very smooth, which is corresponding to the SEM images of S400 (Fig. 3a) and S450 (Fig. 3c) samples. But when the temperature reaches 500  $^{\circ}\text{C}$ , the surface area reaches to 57.05 m<sup>2</sup> g<sup>-1</sup> dramatically, which can be ascribed to the appearance of the pores on the surface of the CFs. However, when the temperature continues to raise, the surface area decreases inversely, which is caused by the increase of the pore diameter. All these results are consistent to the variation of pore size, as shown in Fig. S3.



**Scheme 1** Schematic representation of the formation process of the TiO<sub>2</sub>/porous CFs composite by a simple self-template method



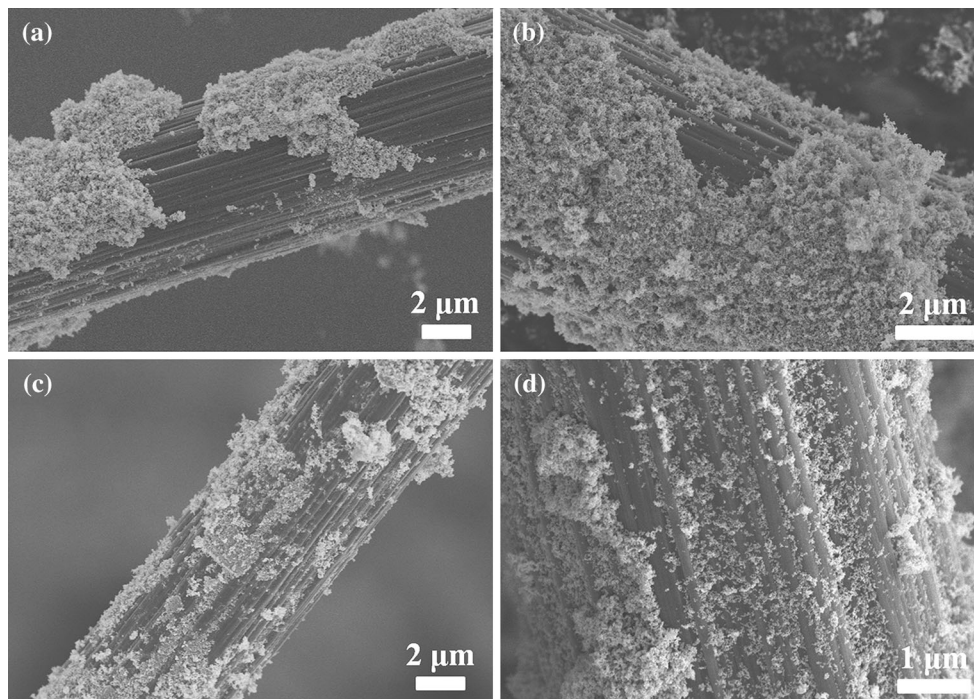


**Fig. 1** SEM images of  $\text{TiO}_2/\text{CFs}$  composites with different additives were added: **a** PEG, **b** no additive, **c** and **d**  $\text{CH}_3\text{COOH}$

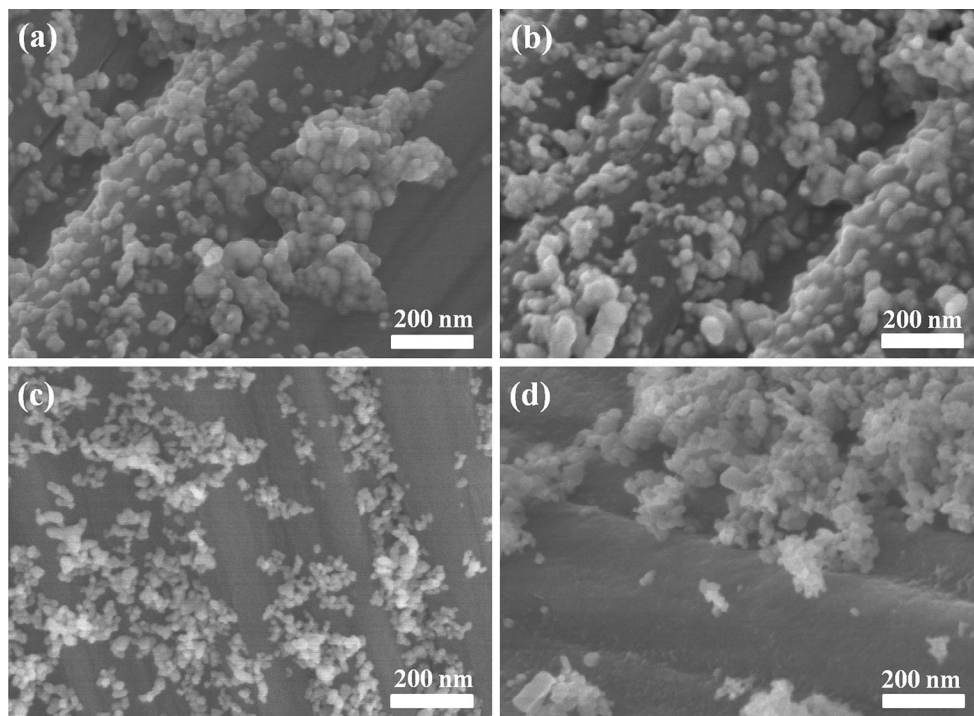


**Fig. 2** The high-resolution SEM images of  $\text{TiO}_2/\text{CFs}$  composites: **a** and **b** used PEG as additive, **c** and **d** used  $\text{CH}_3\text{COOH}$  as additive

Figure 4a shows the XRD patterns of all the samples. The peaks at  $2\theta$  values of 25.3, 37.8, 48.0, 53.9, 55.1, 62.7, 68.8, 70.3, and 75.0° correspond to the crystal planes of (101), (004), (200), (105), (211), (204), (116), (220), and

(215) of the anatase phase  $\text{TiO}_2$  (JCPDS No. 21-1272), respectively. In addition, characteristic diffraction peaks at 27.4, 36.1, 41.2, and 56.7° are also observed, which are attributed to the (110), (101), (111), and (220) planes of the

**Fig. 3** SEM images of TiO<sub>2</sub>/CFs composites and CFs after calcined at high temperatures: **a**, **b** 400 °C; **c**, **d** 450 °C; **e**, **f** 500 °C; **g**, **h** 550 °C; and **i**, **j** 600 °C, respectively

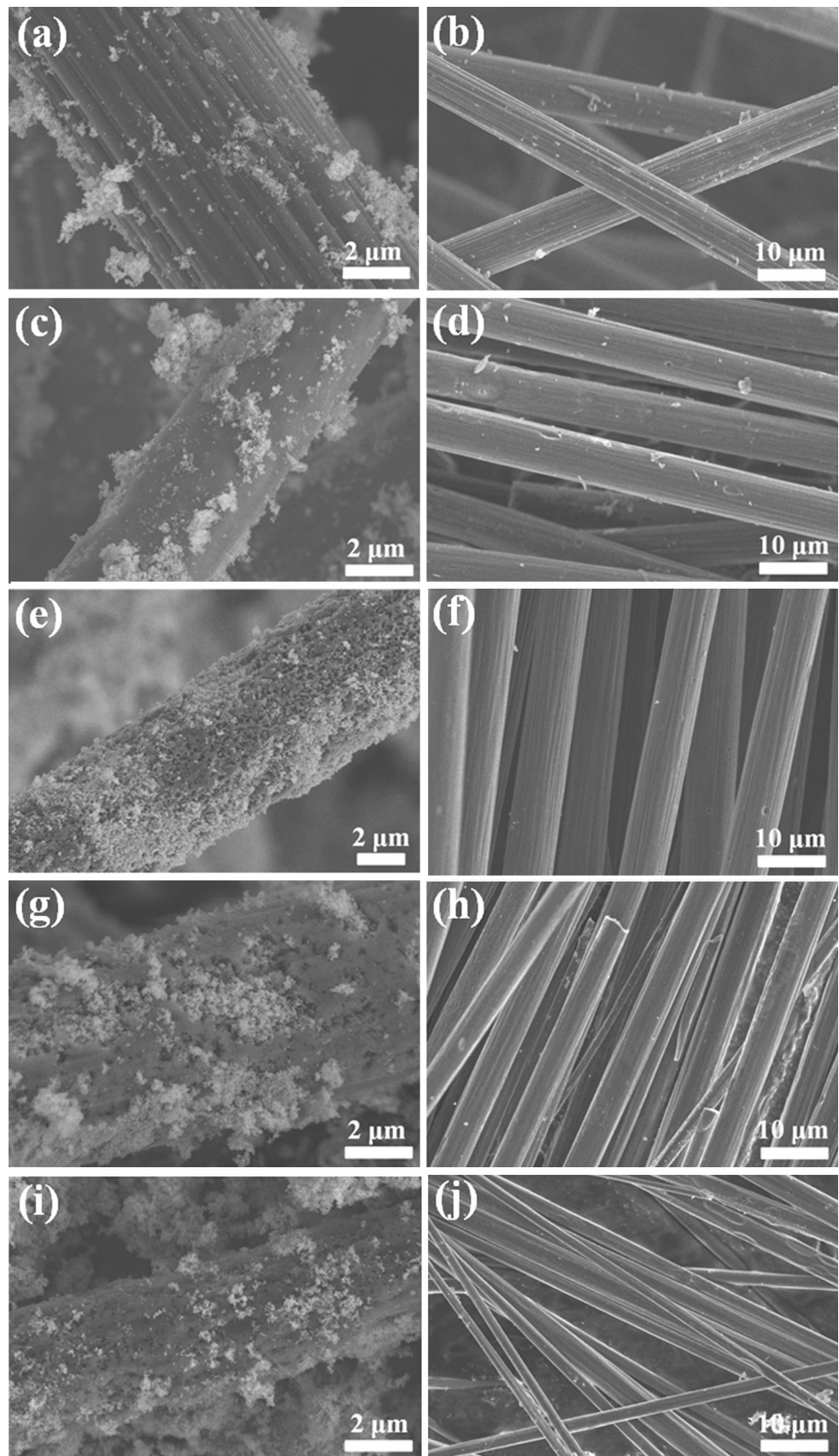


**Table 1** BET data of all the samples

Samples	CF/P25	S400	S450	S500	S550	S600
BET surface area ( $\text{m}^2 \text{g}^{-1}$ )	41.3894	33.9869	27.4043	57.0564	51.5774	38.3238
Total pore volume ( $\text{cm}^3 \text{g}^{-1}$ ) <sup>a</sup>	0.316247	0.277359	0.150237	0.175693	0.336487	0.326478
Pore diameter (nm) <sup>b</sup>	30.5	32.6	21.9	12.3	26.1	34.1

<sup>a</sup> Single-point total pore volume of the pores at  $P/P_0$ , 0.95

<sup>b</sup> BJH desorption average pore diameter

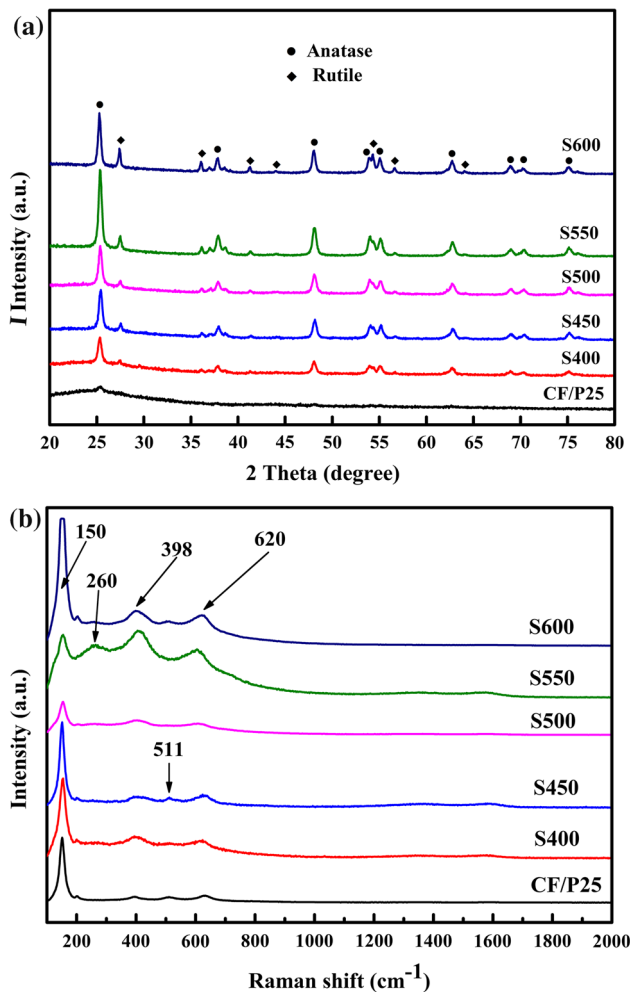


**Fig. 4** XRD patterns and Raman spectra of all the P25/CFs composites

rutile phase  $\text{TiO}_2$  (JCPDS No. 21-1276). It can be obviously seen that the crystallinity of P25 is improved after calcination treatment. The weight ratio of anatase ( $f_A$ ) in the mixture can be obtained from the Eq. (1): [32]

$$f_A = \frac{1}{1 + 1.26 \frac{I_R}{I_A}} \quad (1)$$

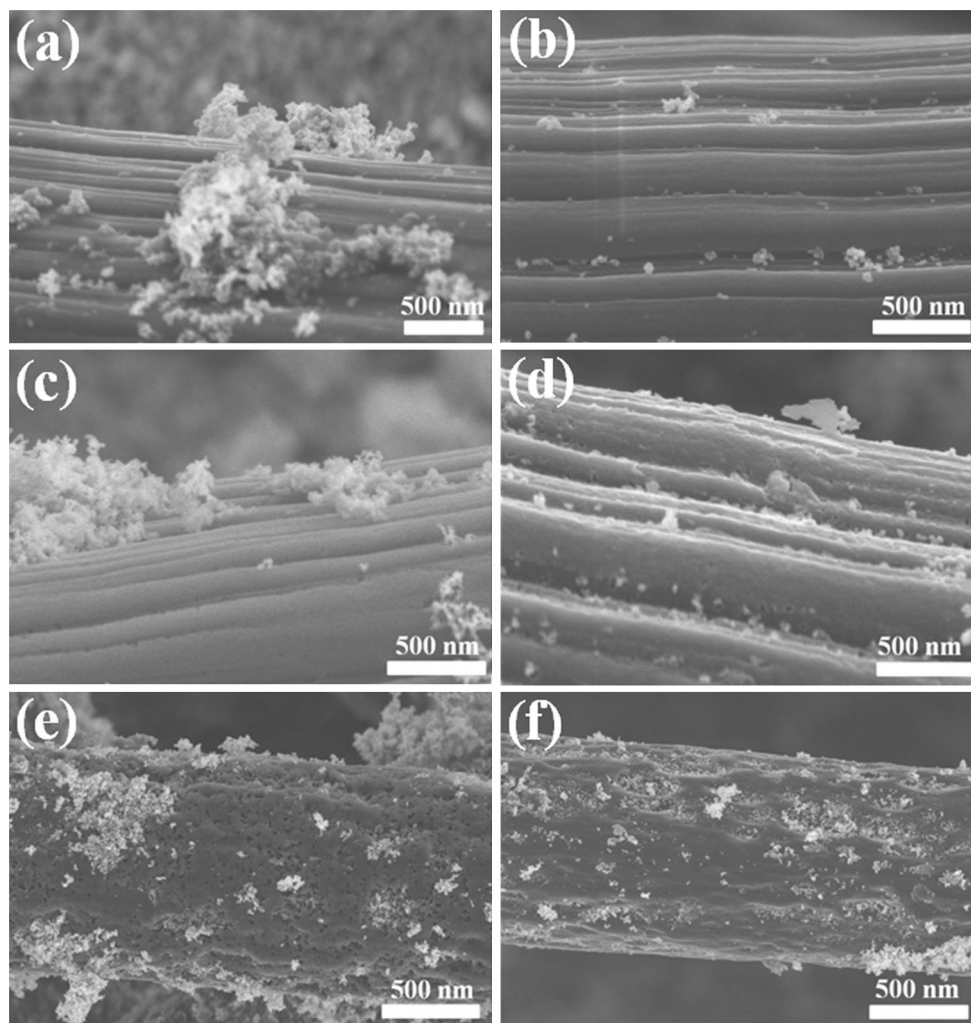
where  $I_R$  is the intensity of the strongest rutile reflection, and  $I_A$  is the intensity of the strongest anatase reflection. For the original P25 particle,  $f_A$  is 0.75, which agrees well with the characteristic of commercial P25. For the S400, S450, S500, and S600 samples, the  $f_A$  is 0.64, 0.69, 0.71, and 0.65, respectively, which are all lower than the value of P25, demonstrating that the rutile phase increased after calcination treatment. However, the  $f_A$  of S550 sample (0.76) is higher than that of P25, implying that the carbon plays an important role in the phase transition process caused by calcination treatment.

Raman spectrum is another useful technique to analyze the change of composition and phase. Here we used the JY-HR800 microdomain Raman spectroscopy to measure the Raman spectra of all the samples. Due to the small spot (diameter less than  $1 \mu\text{m}$ ), the test area can be effectively positioned on the P25 clusters, which can achieve the individual observation of the change of  $\text{TiO}_2$ . The characteristic modes of anatase  $\text{TiO}_2$  are clearly observed in the Raman spectra of all the samples (Fig. 4b). The peaks centered at around 150, 398, 511, and  $620 \text{ cm}^{-1}$  are associated with  $E_{g(1)}$ ,  $B_{1g}$ ,  $A_{1g}$ , and  $E_{g(2)}$  mode of anatase  $\text{TiO}_2$ , respectively [33, 34]. The band at  $260 \text{ cm}^{-1}$  is corresponding to the rutile  $\text{TiO}_2$ . Another two weak peaks centered at around 1348 and  $1575 \text{ cm}^{-1}$  are consistent with the D and G peaks of the carbon. Based on the above Raman results, it can be confirmed that the phase has little change.

In order to confirm that physical adsorption is not the only action form between  $\text{TiO}_2$  and CFs, simple ultrasonic cleaning tests were carried out for the S400, S550, and original P25/CFs samples. The corresponding SEM images of the samples before and after test are shown in Fig. 5a, c, e and b, d, f, respectively. After ultrasonic cleaning, only few P25 particles attach on the CFs for the original P25/CFs (Fig. 5b) and S400 (Fig. 5d) samples, while lots of P25 particles still exist on the surface of CFs for the S550 sample (Fig. 5f), especially on the bottom of the pits. To further shed some light onto the surface chemical composition of the samples, the interface between  $\text{TiO}_2$  and carbon was investigated in detail using XPS measurements. Figure 6 shows the XPS spectra of the S400 and S550



**Fig. 5** The SEM images of TiO<sub>2</sub>/CFs composites calcined at different temperatures before and after ultrasonic cleaning: **a**, **b** unannealed sample; **c**, **d** sample S400; and **e**, **f** sample S550, respectively

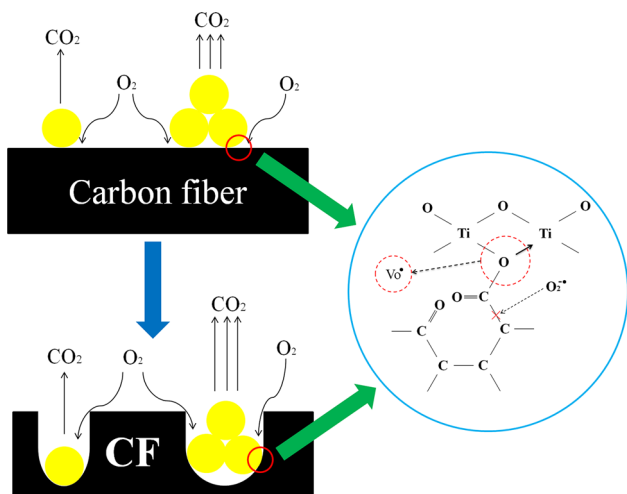
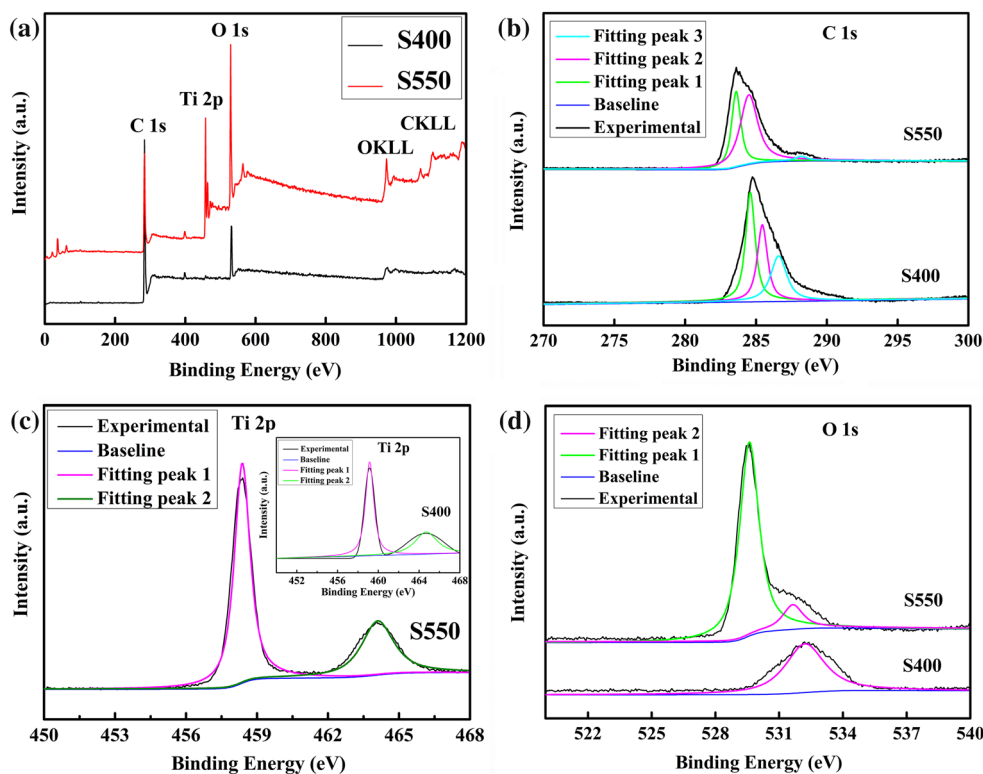


sample. Figure 6a depicts the full survey spectra of the samples. The elements of C, Ti, and O can be clearly identified in the S550 sample but there are no obvious Ti element-related peaks in the S400 sample due to the low amount of TiO<sub>2</sub> after ultrasonic cleaning. High-resolution scans show that the exact binding energies of these elements are slightly different, as revealed in panels from b to d. From Fig. 6b, for the S400 sample, there are three major peaks centered at 285, 285.4, and 286 eV, which may be assigned to the 1 s electrons of sp<sup>3</sup> hybridized carbon (C–C) and sp<sup>2</sup> hybridized carbon (C=C), and the formation of C–OH bond, respectively [35]. For the S550 sample, the peak of C=C is still existed at 285.4 eV, and other two peaks appear at around 283.6 eV and 288.2 eV, which may be related to the formation of Ti–O–C bond and C=O bond. Both the samples have two peaks at 458.4 and 464 eV corresponding to Ti<sup>4+</sup> atoms in TiO<sub>2</sub> (as shown in Fig. 6c) [36]. For the O 1s electrons (as shown in Fig. 6d), both the samples exhibit a peak at around 532 eV corresponding to the hydroxyl O on the TiO<sub>2</sub> surface while the S550 sample

has a another strong peak at 529.6 eV, which is assigned to oxygen bonded to Ti [37].

From the above results, the formation mechanism of TiO<sub>2</sub>/porous CFs composite can be deduced. The oxygen molecules in air would be activated on the surface of TiO<sub>2</sub> particles at relatively low temperature because the oxygen vacancy can trap an electron, which has been reported in many literatures [38, 39]. The activated oxygen molecules react with carbon and TiO<sub>2</sub> leading to the formation of C–O bond and Ti–O bond. Then the C–O bond would further react with the activated oxygen molecules to form the C=O bond as the calcination temperature increases, which can be observed from the changes of XPS spectra. Finally, the carbon dioxide forms and escapes from the interface, as schematically illustrated in Scheme 2. Because the amount of activated oxygen formed at the interface between TiO<sub>2</sub> and CF is larger than other places on the CFs, the etching rate of carbon attached with TiO<sub>2</sub> is increased significantly, leading to the formation of the pores. Naturally, the pore size is determined by the size of the TiO<sub>2</sub> clusters. In the

**Fig. 6** a XPS survey spectra of  $\text{TiO}_2/\text{CFs}$  composites calcined at 400 and 550 °C, and high-resolution scans of the binding energies of b C 1s, c Ti 2p, d O 1s electrons in the composites



**Scheme 2** A schematic showing the etching process of the CFs at high temperature with  $\text{TiO}_2$  particles as catalyst

formation process, the  $\text{TiO}_2$  clusters act as either catalyst or template. In summary, we prepared a  $\text{TiO}_2/\text{porous CFs}$  composite by a simple self-template method.

#### Photocatalytic activity

Photocatalytic activities of the  $\text{TiO}_2/\text{porous CFs}$  composites were evaluated by the photo-degradation of RhB aqueous solutions. The dye adsorption rates of all the

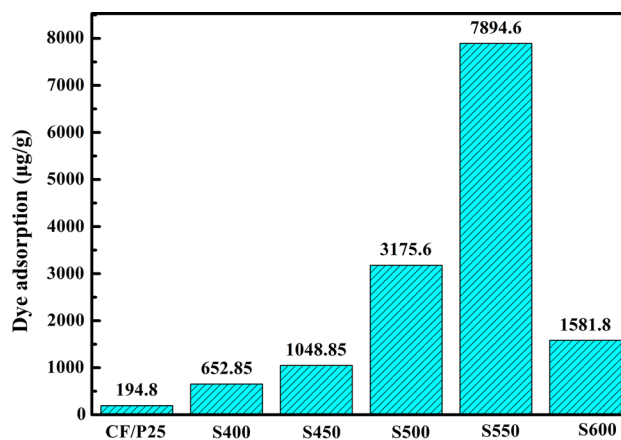


**Fig. 7** The dye adsorption rate of all the  $\text{TiO}_2/\text{CFs}$  composites

samples are displayed in Fig. 7. It can be observed that the amount of residual RhB in the sample solutions after dark treatment for 60 min decreases with the increase of the calcination temperature, except the S600 sample. This result reflects that the porous structure could improve the adsorption ability of the  $\text{TiO}_2/\text{CFs}$  composites. The time evolution of the dye concentration in different catalysts solution is shown in Fig. 8a, where the entire reaction time does not include the time for adsorption equilibrium. The RhB concentration (%) after several intervals of time could be estimated using the Eq. (2):



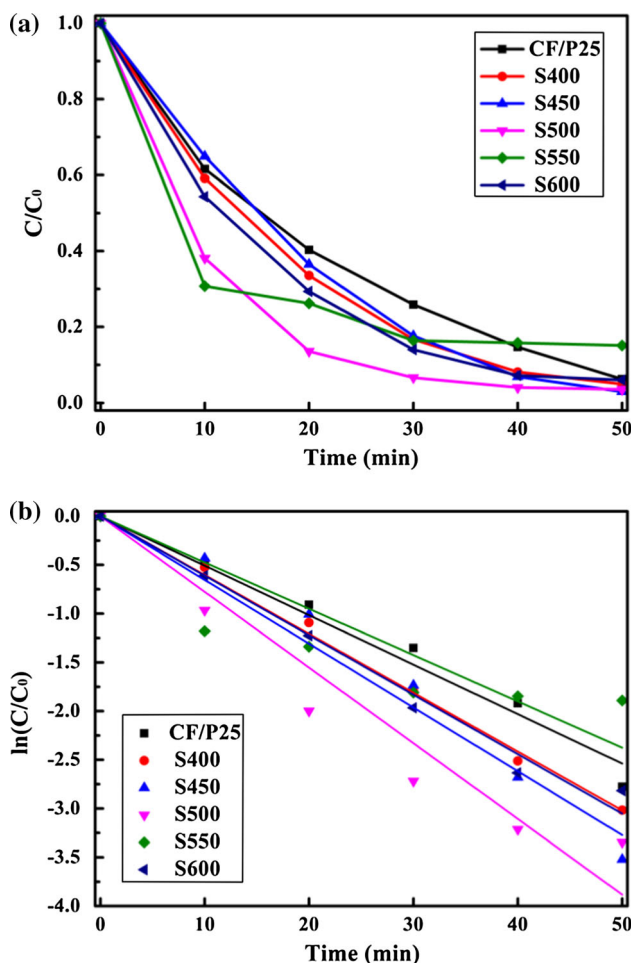
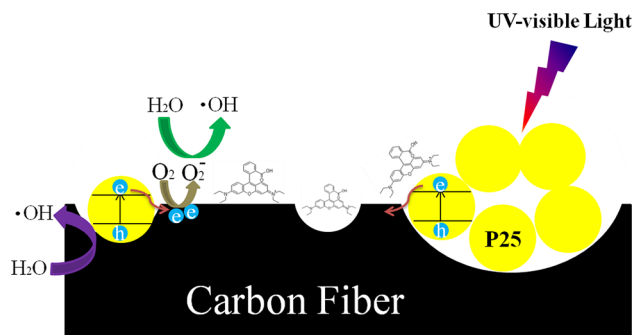


**Fig. 8** **a** Photocatalytic degradation of rhodamine B with TiO<sub>2</sub>/CFs composites as photocatalysts under UV light and **b** kinetics of RhB decolourisation with different photocatalysts

$$\% \text{ RhB concentration} = (C/C_0) \times 100\% \quad (2)$$

where  $C_0$  is the initial RhB absorbance at 554 nm and  $C$  is the absorbance after several intervals of time ( $t$ ). As shown in Fig. 8a, the removal rate of dye is enhanced after the calcination of TiO<sub>2</sub>/CFs composites. Due to the effect of adsorption, the amount of residual dye in solution cannot be regarded as a direct evidence to demonstrate the catalytic efficiency. The apparent rate constant can be chosen as the basic kinetic parameter for the comparison of different photocatalysts' photocatalytic activities. The obtained apparent rate constants of different samples are 0.05076, 0.06038, 0.06542, 0.07765, 0.04735, and 0.06296 min<sup>-1</sup> for the P25/CFs, S400, S450, S500, S550, and S600 samples, respectively (as shown in Fig. 8b). It can be seen that all the samples show enhanced activity compared to pure P25 (0.03302 min<sup>-1</sup>, as shown in Fig. S4 (Supporting information)). The enhancement can be ascribed to the synergistic effect between TiO<sub>2</sub> and carbon,



**Scheme 3** Schematic illustrations of the synergistic effect in the photocatalysts of TiO<sub>2</sub>/porous CFs composites due to the unique structure of porous CFs

which can hinder the recombination of photo-generated electrons and holes. Scheme 3 illustrates the process diagram of RhB degradation caused by the TiO<sub>2</sub>/porous CFs composites. Theoretically, the dye in solution cannot sufficiently contact with P25 particles due to their immobilization on the CFs surface, and the photocatalytic efficiency would be seriously weakened. But in the experiment, the dye would be adsorbed on the surface of the composite due to the existence of the porous structure, which can increase the encounter rate of dye and hydroxyl radicals ( $\cdot\text{OH}$ ). But too much adsorbed dye would cause the shielding effect and decrease the light absorption of TiO<sub>2</sub> [40]. This may be the major reason that the S550 sample has the worst catalytic activity. The catalytic activity of the S600 sample may be influenced by the disappearance of the porous structure caused by the excessive etching, as shown in Fig. S5 (Supporting information). The role of CFs in the photocatalysis maybe is as not only a substrate to support the TiO<sub>2</sub> particles, but also an electron collector to retard the recombination of photo-induced charge carries and prolong electron lifetime.

### Conclusions

In summary, TiO<sub>2</sub>/porous CFs composites were fabricated by a simple self-template method. During the calcinations process, the P25 clusters as catalyst can enhance the etch reaction rate between carbon and oxygen. It can also be considered as a template, which would determine the size and sites of the pores. Due to the unique porous structure, the TiO<sub>2</sub>/porous CFs composites exhibit excellent adsorption ability, and enhanced photocatalytic activity. But too much adsorbed dye also reduces its activity because of the shielding effect. Combining the advantages of TiO<sub>2</sub> and CFs, the composite can be applied in many fields, such as water splitting, lithium ion batteries, especially the application of the photocatalytic degradation of organic pollutants.

**Acknowledgements** This project was supported by the National Natural Science Foundation of China (Nos. 61176058, 51302122), the National Natural Science Foundation of China and Chinese Academy of Sciences Joint Fund of Research Utilizing Large-scale Scientific Facilities (No. U1232121) and the Program for Changjiang Scholars and Innovative Research Team in University (Grant No: IRT1251).

## References

- Gomathi Devi L, Girish Kumar S, Mohan Reddy K, Muni-krishnappa C (2009) Photo degradation of methyl orange an azo dye by advanced Fenton process using zero valent metallic iron: influence of various reaction parameters and its degradation mechanism. *J Hazard Mater* 164:459–467
- Tang J, Chen S, Xu Y, Zhong W, Ma M, Wang Z (2012) Calibration and field performance of triolein embedded acetate membranes for passive sampling persistent organic pollutants in water. *Environ Pollut* 164:158–163
- El Saliby I, Erdei L, Kim JH, Shon HK (2013) Adsorption and photocatalytic degradation of methylene blue over hydrogen-titanate nanofibres produced by a peroxide method. *Water Res* 47:4115–4125
- Auta M, Hameed BH (2012) Modified mesoporous clay adsorbent for adsorption isotherm and kinetics of methylene blue. *Chem Eng J* 198–199:219–227
- Machida M, Fotoohi B, Amamo Y, Ohba T, Kanoh H, Mercier L (2012) Cadmium(II) adsorption using functional mesoporous silica and activated carbon. *J Hazard Mater* 221–222:220–227
- Wu Z, Cheng Z, Ma W (2012) Adsorption of Pb(II) from glucose solution on thiol-functionalized cellulosic biomass. *Bioresour Technol* 104:807–809
- Buchel R, Pratsinis SE, Baiker A (2012) Mono- and bimetallic Rh and Pt NSR-catalysts prepared by controlled deposition of noble metals on support or storage component. *Appl Catal B Environ* 113–114:160–171
- Celorrío V, Montes de Oca MG, Plana D, Moliner R, Fermín DJ, Lázaro MJ (2012) Electrochemical performance of Pd and Au–Pd core–shell nanoparticles on surface tailored carbon black as catalyst support. *Int J Hydrogen Energy* 37:7152–7160
- Ben-Moshe T, Dror I, Berkowitz B (2009) Oxidation of organic pollutants in aqueous solutions by nanosized copper oxide catalysts. *Appl Catal B Environ* 85:207–211
- Yan S, Wang J, Gao H et al (2013) Zinc gallogermanate solid solution: a novel photocatalyst for efficiently converting CO<sub>2</sub> into solar fuels. *Adv Funct Mater* 23:1839–1845
- Colmenares JC, Luque R (2014) Heterogeneous photocatalytic nanomaterials: prospects and challenges in selective transformations of biomass-derived compounds. *Chem Soc Rev* 43:765–778
- Joo JB, Lee I, Dahl M, Moon GD, Zaera F, Yin Y (2013) Controllable synthesis of mesoporous TiO<sub>2</sub> hollow shells: toward an efficient photocatalyst. *Adv Funct Mater* 23:4246–4254
- Wang Y, Zhang Y-Y, Tang J et al (2013) Simultaneous etching and doping of TiO<sub>2</sub> nanowire arrays for enhanced photoelectrochemical performance. *ACS Nano* 7:9375–9383
- He Y, Basnet P, Murph SE, Zhao Y (2013) Ag nanoparticle embedded TiO<sub>2</sub> composite nanorod arrays fabricated by oblique angle deposition: toward plasmonic photocatalysis. *ACS Appl Mater Interfaces* 5:11818–11827
- Teng F, Li M, Gao C et al (2014) Preparation of black TiO<sub>2</sub> by hydrogen plasma assisted chemical vapor deposition and its photocatalytic activity. *Appl Catal B Environ* 148–149:339–343
- Carneiro JO, Azevedo S, Fernandes F et al (2014) Synthesis of iron-doped TiO<sub>2</sub> nanoparticles by ball-milling process: the influence of process parameters on the structural, optical, magnetic, and photocatalytic properties. *J Mater Sci* 49:7476–7488. doi:10.1007/s10853-014-8453-3
- Lee D, Kim H-B, Yu S, Kim HJ, Lee WI, Jang D-J (2014) Facile fabrication of anatase TiO<sub>2</sub> nanotube arrays having high photocatalytic and photovoltaic performances by anodization of titanium in mixed viscous solvents. *J Mater Sci* 49:3414–3422. doi:10.1007/s10853-014-8051-4
- Wang B, Li C, Cui H, Zhang J, Zhai J, Li Q (2014) Shifting mechanisms in the initial stage of dye photodegradation by hollow TiO<sub>2</sub> nanospheres. *J Mater Sci* 49:1336–1344. doi:10.1007/s10853-013-7817-4
- Cheng X, Liu H, Chen Q, Li J, Wang P (2014) Preparation of graphene film decorated TiO<sub>2</sub> nano-tube array photoelectrode and its enhanced visible light photocatalytic mechanism. *Carbon* 66:450–458
- Chen P, Gu L, Xue X, Li M, Cao X (2010) Engineering the growth of TiO<sub>2</sub> nanotube arrays on flexible carbon fibre sheets. *Chem Commun* 46:5906–5908
- Guo W, Zhang F, Lin C, Wang ZL (2012) Direct growth of TiO<sub>2</sub> nanosheet arrays on carbon fibers for highly efficient photocatalytic degradation of methyl orange. *Adv Mater* 24:4761–4764
- Woan K, Pyrgiotakis G, Sigmund W (2009) Photocatalytic carbon-nanotube-TiO<sub>2</sub> composites. *Adv Mater* 21:2233–2239
- Xing M, Qi D, Zhang J et al (2012) Super-hydrophobic fluorination mesoporous MCF/TiO<sub>2</sub> composite as a high-performance photocatalyst. *J Catal* 294:37–46
- Daranyi M, Csesznok T, Kukovecz A et al (2011) Layer-by-layer assembly of TiO<sub>2</sub> nanowire/carbon nanotube films and characterization of their photocatalytic activity. *Nanotechnology* 22:195701
- Yuan R, Guan R, Zheng J (2005) Effect of the pore size of TiO<sub>2</sub>-loaded activated carbon fiber on its photocatalytic activity. *Scr Mater* 52:1329–1334
- Shi J, Zheng J, Wu P, Ji X (2008) Immobilization of TiO<sub>2</sub> films on activated carbon fiber and their photocatalytic degradation properties for dye compounds with different molecular size. *Catal Commun* 9:1846–1850
- Wu X, Yin S, Dong Q et al (2013) Synthesis of high visible light active carbon doped TiO<sub>2</sub> photocatalyst by a facile calcination assisted solvothermal method. *Appl Catal B Environ* 142–143:450–457
- Zhang G, Teng F, Wang Y et al (2013) Preparation of carbon–TiO<sub>2</sub> nanocomposites by a hydrothermal method and their enhanced photocatalytic activity. *RSC Adv* 3:24644–24649
- Zhang G, Teng F, Zhao C et al (2014) Enhanced photocatalytic activity of TiO<sub>2</sub>/carbon@TiO<sub>2</sub> core–shell nanocomposite prepared by two-step hydrothermal method. *Appl Surf Sci* 311:384–390
- Imae T, Muto K, Ikeda S (1991) The pH dependence of dispersion of TiO<sub>2</sub> particles in aqueous surfactant solutions. *Colloid Polym Sci* 269:43–48
- Barbé CJ, Arendse F, Comte P et al (1997) Nanocrystalline titanium oxide electrodes for photovoltaic applications. *J Am Ceram Soc* 80:3157–3171
- Spurr RA, Myers H (1957) Quantitative analysis of anatase-rutile mixtures with an X-ray diffractometer. *Anal Chem* 29:760–762
- Zhang W, He Y, Zhang M, Yin Z, Chen Q (2000) Raman scattering study on anatase TiO<sub>2</sub> nanocrystals. *J Phys D Appl Phys* 33:912–916
- Xiang Q, Yu J, Jaroniec M (2012) Synergetic effect of MoS<sub>2</sub> and graphene as cocatalysts for enhanced photocatalytic H<sub>2</sub> production activity of TiO<sub>2</sub> nanoparticles. *J Am Chem Soc* 134:6575–6578
- Hung M-C, Yuan S-Y, Hung C-C, Cheng C-L, Ho H-C, Ko T-H (2014) Effectiveness of ZnO/carbon-based material as a catalyst for photodegradation of acrolein. *Carbon* 66:93–104

36. Zheng ZQ, Zhou XP, Damjanovic D (2013) Reduction of  $Ti^{4+}$  to  $Ti^{3+}$  in boron-doped  $BaTiO_3$  at very low temperature. *J Am Ceram Soc* 96:3504–3510
37. Lin Y-T, Weng C-H, Lin Y-H, Shiesh C-C, Chen F-Y (2013) Effect of C content and calcination temperature on the photocatalytic activity of C-doped  $TiO_2$  catalyst. *Sep Purif Technol* 116:114–123
38. Nakamura I, Negishi N, Kutsuna S, Ihara T, Sugihara S, Takeuchi K (2000) Role of oxygen vacancy in the plasma-treated  $TiO_2$  photocatalyst with visible light activity for NO removal. *J Mol Catal A: Chem* 161:205–212
39. Long J, Chang H, Gu Q et al (2014) Gold-plasmon enhanced solar-to-hydrogen conversion on the 001 facets of anatase  $TiO_2$  nanosheets. *Energy Environ Sci* 7:973–977
40. Hsiao Y-C, Wu T-F, Wang Y-S, Hu C-C, Huang C (2014) Evaluating the sensitizing effect on the photocatalytic decoloration of dyes using anatase- $TiO_2$ . *Appl Catal B Environ* 148–149:250–257